Supplementary Information

Manipulating cation solvation equilibrium in sole-solvent electrolyte for fast-charging and wide-temperature-range sodium metal batteries

Yumei Liu[1,2,*], Yongqing Gong[3], Tianyu Huang[3], Chenxi Zheng[2], Kaier Shen[2], Yingjing Yan[2], Menghao Yang[3,*], Quanquan Pang[2,*]

[1]*School of Chemistry and Chemical Engineering, Chongqing University, Chongqing 401331, China*

[2]*Beijing Key Laboratory for Theory and Technology of Advanced Battery Materials, School of Materials Science and Engineering, Peking University, Beijing 100871, China*

[3]*School of Materials Science and Engineering, Tongji University, Shanghai 201804, China*

*Corresponding author: Yumei Liu, *School of Chemistry and Chemical Engineering, Chongqing University, Chongqing 401331, China; Beijing Key Laboratory for Theory and Technology of Advanced Battery Materials, School of Materials Science and Engineering, Peking University, Beijing 100871, China;* liuyumei@cqu.edu.cn. *Corresponding author: Menghao Yang, *School of Materials Science and Engineering, Tongji University, Shanghai 201804, China,* menghaoyoung@tongji.edu.cn. *Corresponding author: Quanquan Pang, *Beijing Key Laboratory for Theory and Technology of Advanced Battery Materials, School of Materials Science and Engineering, Peking University, Beijing 100871, China,* qqpang@pku.edu.cn.

Contents

Supplementary Table 1. Physicochemical properties of the conventionally used organic solvents in SIBs and LIBs[1-10].

Organic solvents	Donor number (kcal mol^{-1})	Freezing point (°C)	Boiling point (°C)	Dielectric constant (25 °C)	Viscosity (25 °C, cP)
MA (methyl acetate)	16.5	−98	56	6.67	0.37
THF (tetrahydrofuran)	20	−108.5	66	7.58	0.59 (20 °C)
2-MeTHF (2-Methyltetrahydrofuran)	~18-19	−136	80	6.2	0.60 (20 °C)
3-MeTHF (3-Methyltetrahydrofuran)	~18-20	−137	86-87	~ 8–9	~ 1.2–1.5
DOL (1,3-Dioxolane)	21.2	−95	75.6	7.34	0.589
EA (ethyl acetate)	17.1	−84	102	6	0.45
EC (ethylene carbonate)	16.4	36.4	248	89.78	1.90
PC (propylene carbonate)	15.0	−48.8	242	64.92	2.53
SN (succinonitrile)	-	50−54	266	54	-
AN (acetonitrile)	14.1	−44	81.6	37.5	0.35
DME (1,2-Dimethoxyethane)	20	−58	86	5.5	1.1
DEGDME (diethylene glycol dimethyl ethe)	-	−64	162	7.18	1.06
CPME (cyclopentyl methyl ether)	-	-140	106	4.7	0.55 (20 °C)
DMC (dimethyl carbonate)	17.2	4.6	991	3.1	0.63
DMF (dimethyl formamide)	26.6	−60.4	153	0.8	37
DMSO (dimethyl sulfoxide)	29.8	18.4	189	46.7	1.99

Supplementary Note 1: Owing to the absence of comprehensive experimental datasets for 3-MeTHF in previous reports, the solvent parameters of 3-methyltetrahydrofuran (3-MeTHF), including dielectric constant, boiling point, and viscosity, were derived through computational estimation based on its structural isomer 2-methyltetrahydrofuran, tetrahydrofuran analogues,

and cross-referencing established physicochemical databases (e.g., NIST Chemistry WebBook, PubChem).

The solvation Gibbs free energy (ΔG) of cations is governed by the enthalpic and entropic interactions between cations, the solvent and other ions (e.g., anions) in electrolyte. Furthermore, the solvation of Na^+ is driven largely by strong enthalpic interactions with electron-donating groups on solvent molecules. The strength of this interaction is quantified by the Gutmann donor number (DN), which serves as a key parameter for predicting solvent-cation and anion-cation interactions[11]. Therefore, DN mainly governs the ΔG values through the cation-solvent interactions. In our study, the solvents of THF, 2-MeTHF and 3-MeTHF all featuring appropriate DN (< 21 kcal mol^{-1}) are selected to enable the efficient ionic conductivity (Fig. 1c, in the main text) and low energy barriers of Na^+ desolvation (Fig. 2f, in the main text), which is adequate for high-rate cell operation. Hence, we view the low dielectric constant not as a weakness, but as a key design parameter that configures a solvation shell with enhanced anion participation for robust interphases, which is more critical for high-performance sodium metal batteries than maximizing bulk ionic conductivity.

As a solvent, 3-MeTHF is flammable. Our work aimed to demonstrate the Na^+ solvation chemistry with the balanced Na^+-solvent and Na^+-anion interactions is critical for the cells with fast-charging capability and wide-temperature performance. Hence, the question is how the presence of a methyl group and its specific position on the THF ring influences the interactions between Na^+-solvent and Na^+-anion. Compared to the 2-substituted molecule (i.e., 2-MeTHF), the methyl group at the 3-position creates a distinct electronic structure. We speculate that this would lead to a subtle but pivotal difference in its electron-donating ability, thereby balancing the competitive interactions between Na^+-solvent and Na^+-anion more effectively. Our subsequent experimental and theoretical results confirm that the 3-MeTHF demonstrates a high ability to configure a balanced anion-solvent-coordinated solvation shell for the enhanced fast-charging capability and wide-temperature performance.

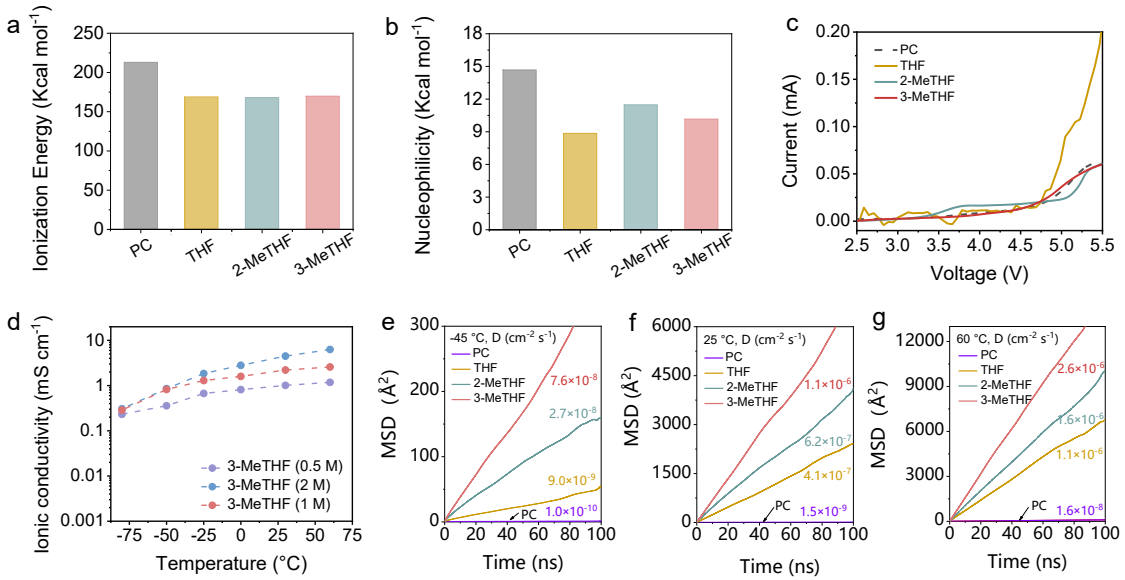

Supplementary Fig. 1 Quantum chemical analysis of solvent molecules stability and physicochemical properties of 3-MeTHF. (a) The molecule of 3-MeTHF showing the slightly higher ionization energy compared to THF and 2-MeTHF, demonstrating its enhanced oxidation stability. (b) The lower nucleophilicity of 3-MeTHF molecule compared to 2-MeTHF, indicating the less possibility of reduction decomposition. These favorable electronic protection mechanisms, i.e., elevated oxidation barrier and reduced reduction propensity, establish 3-MeTHF as an optimal electrolyte solvent. (c) Oxidative stability of the electrolytes as measured by linear sweep voltammetry at a scan rate of 1 mV s^{-1} with the stainless steel as working electrode. Note that the apparent noise in the LSV curve is amplified because the current scale on *y*-axis is small. (d) The ionic conductivity of 3-MeTHF with different salt concentrations over a temperature range from −80 to 60 °C. (e-g) Mean squared displacement (MSD) and the diffusion coefficient of Na^+ in the PC, THF, 2-MeTHF and 3-MeTHF electrolytes under different temperatures of −45 °C (e), 25 °C (f) and 60 °C (g).

Supplementary Note 2: The variation of the ionic conductivity with different salt concentrations is shown in Supplementary Figure 1d. The 2 M electrolyte exhibits the highest ionic conductivity, followed by the 1 M electrolyte, while the 0.5 M electrolyte shows the lowest ionic conductivity. This trend suggests that increasing salt concentration enhances the number of charge carriers, and thereby improves conductivity until the effects such as increased viscosity and ion aggregation show a significant influence at even higher concentrations. We systematically investigated the Na^+ diffusion properties through mean square displacement (MSD) analysis across the four electrolytes, which was calculated from the trajectory after the electrolyte systems reaching equilibrium. As shown in Supplementary Figures 1e-g, compared to PC, THF and 2-MeTHF, the 3-MeTHF electrolyte exhibits the faster ion migration kinetics, as reflected by its significantly steeper MSD slopes at the temperatures of −45 °C, 25 °C and 60 °C. Note that the diffusion coefficient of Na^+ in the 3-MeTHF electrolyte (1.1×10^{-6} cm^2 s^{-1}) is much higher than those in the electrolytes of PC (1.5×10^{-9} cm^2 s^{-1}), THF (4.1×10^{-7} cm^2 s^{-1}) and 2-MeTHF (6.2×10^{-7} cm^2 s^{-1}) at 25 °C. This high transport property stems from its unique solvation structure, and the balanced anion solvent coordination in 3 MeTHF may create a lower energy landscape for Na^+ hopping and reduce the effective activation barrier for diffusion and thus enhance ion mobility.

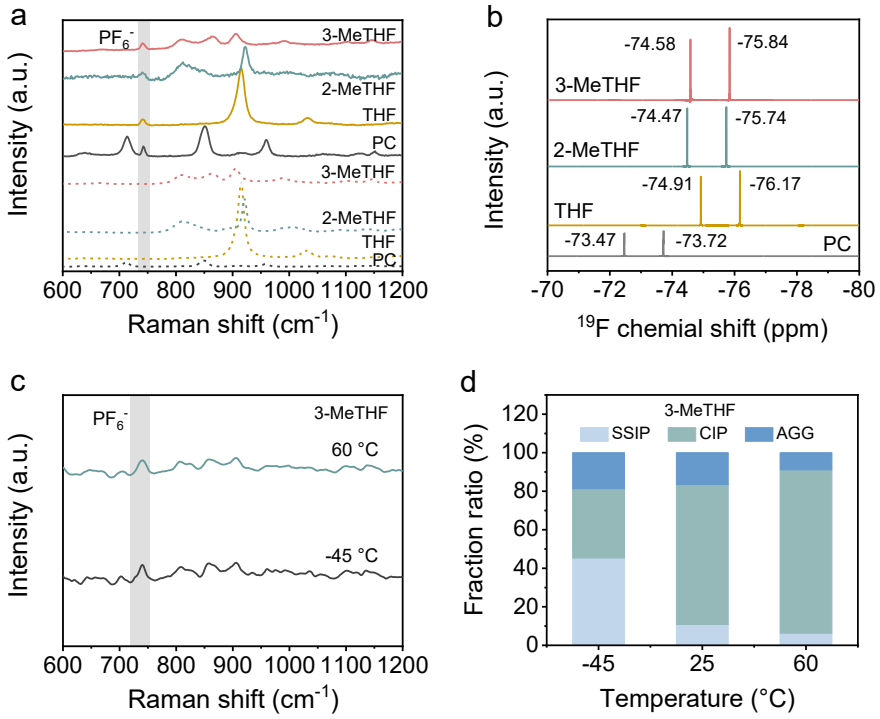

Supplementary Fig. 2 Electrolyte solvation structure analysis of the investigated electrolytes. (a) Raman spectra of pure solvents and formulated electrolytes at 25 °C. (b) ^{19}F NMR spectra showing the increased electron cloud density at phosphorus centers in ethers-based electrolytes in contrast to the PC electrolyte at 25 °C, indicating the strengthened shielding effects from anion-cation coordination. (c) Raman spectra of 3-MeTHF electrolyte at −45 °C and 60 °C. (d) Fraction of anion-induced solvation structures (SSIP/CIP/AGG) at different temperatures.

Supplementary Note 3: For the solvation structure of PC electrolyte, it is critical to integrate findings from NMR, Raman and MD simulations, as conclusions drawn from any single method in isolation may be misleading. For ^{23}Na NMR spectra of PC, a certain degree of anion participation is introduced, but its coordination effect is thermodynamically less favored compared to 3-MeTHF, which is confirmed by the observation in MD simulation (Fig. 2a-d, in the manuscript) and Raman spectra (Fig. 1d, in the manuscript), where both techniques show less contact ion pairs (CIPs) and aggregates (AGGs). This is mainly due to the unique methyl positioning in 3-MeTHF fine-tunes the solvent's electron-donating ability and steric hindrance, thereby establishing an optimally balanced solvation structure where the Na^+-solcvent and Na^+-anion interactions synergistically enhance interfacial kinetics and stability.

Our Raman and simulation results indicate that salt crystallization is effectively mitigated in our 3-MeTHF-based electrolyte. This is attributed to its uniquely balanced solvation structure, which maintains significant solvent participation even at −45 °C (as shown by MD simulations in Fig. 2c and Raman in Supplementary Figure 2d). This structure prevents the anion-cation aggregation that typically initiates crystallization. Meanwhile, the low melting point (−137 °C) and low viscosity (≤1.5 cP, 25 °C) of 3-MeTHF ensure that the electrolyte remains in liquid state, thereby avoiding the phase separation that drives salt precipitation. Besides, the stable ionic conductivity (Fig. 1c) also evidences no salt precipitation occurrence, suggesting the advantage of our electrolyte at low temperatures.

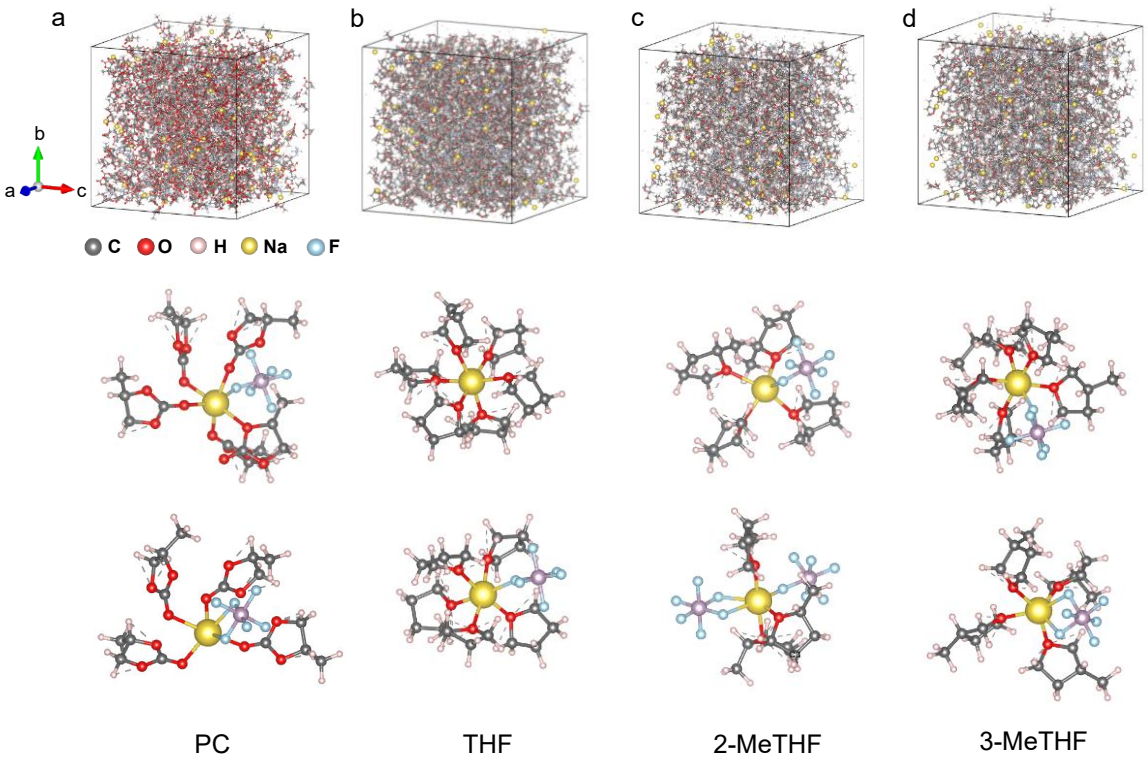

Supplementary Fig. 3 Equilibrated snapshots from trajectory of the MD simulations with representative Na^+ solvation structures in various electrolytes. (a) PC, (b) THF, (c) 2-MeTHF and (d) 3-MeTHF.

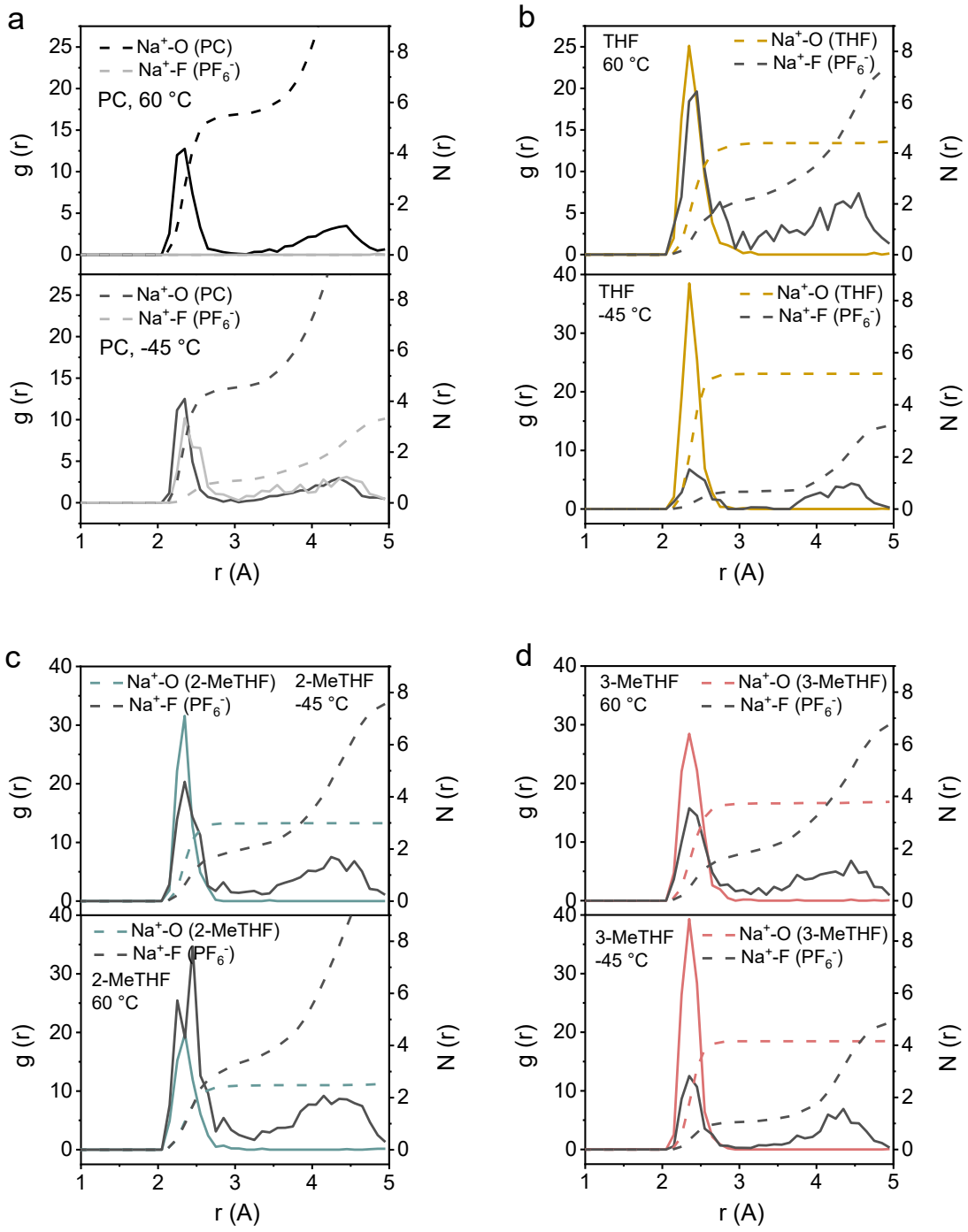

Supplementary Fig. 4 The radial distribution functions (RDFs) and coordination number (CN) analyses at −45 °C and 60 °C. (a-d) The simulation performed on the molecular dynamics (MD) trajectories of the investigated electrolytes, revealing an increase in anion participation with elevating temperature except for the PC electrolyte: (a) PC, (b) THF, (c) 2-MeTHF and (d) 3-MeTHF electrolytes.

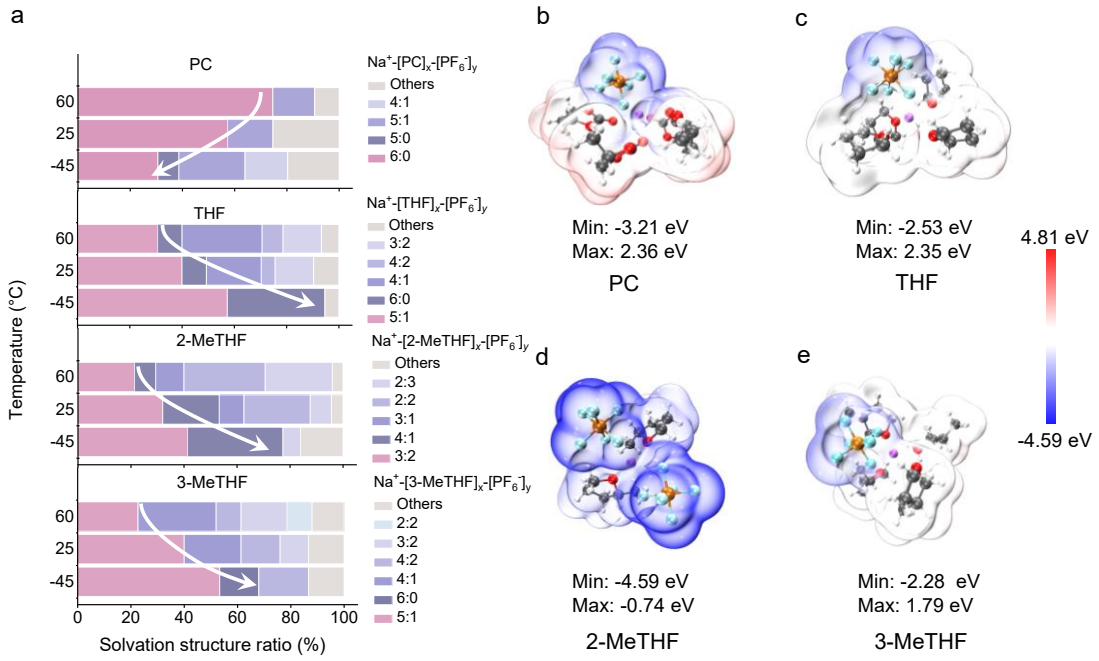

Supplementary Fig. 5 Dominant solvation clusters and the electrostatic potential maps (ESP). (a) Temperature-dependent distribution of dominant solvation clusters at −45/25/60 °C. The annotation close to the colored column, representing the coordinated solvent/anion ratio in solvation structures. (b-e) ESP for the representative solvation clusters simulated from the MD systems, offering a clear visualization of the electrostatic interactions within the solvation environment. (b) PC, (c) THF, (d) 2-MeTHF and (e) 3-MeTHF. The color scheme of atom used is as follows: O (red); C (gray); Na (purple); H (white); P (orange); F (cyan).

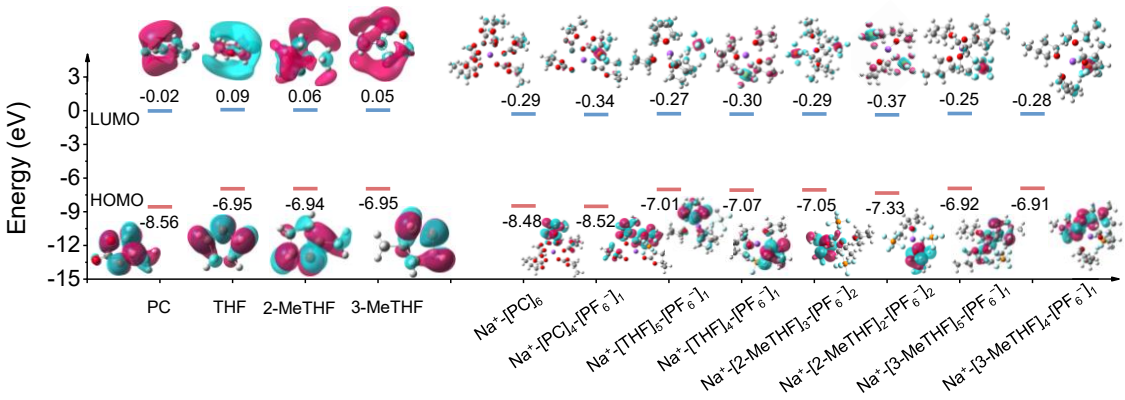

Supplementary Fig. 6 The frontier orbital landscapes of solvent molecules and representative solvation clusters in various electrolytes. The computed energy levels of the Lowest Unoccupied Molecular Orbital (LUMO) and the Highest Occupied Molecular Orbital (HOMO) for these solvent molecules and solvation clusters provide critical insights into their electronic properties. The molecular structures, along with the corresponding frontier orbital isosurfaces, are depicted in the insets, offering a detailed visualization of the electronic environment that plays a key role in interphase stability.

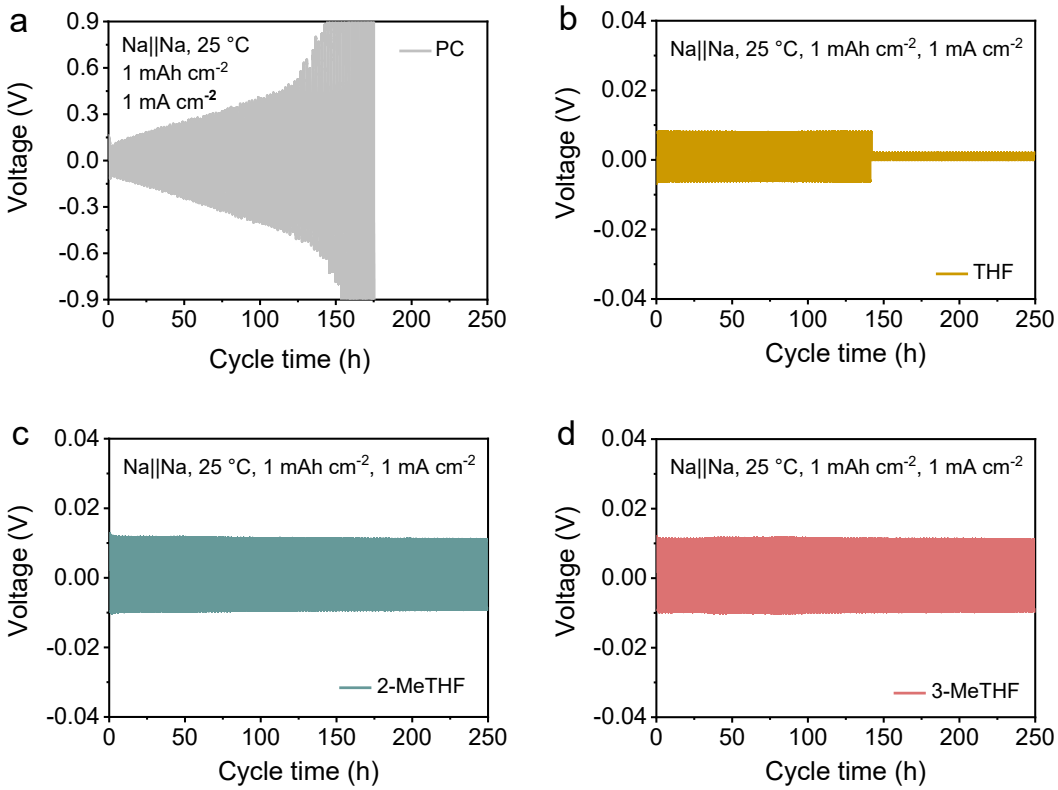

Supplementary Fig. 7 The sodium plating/stripping behavior in symmetric Na||Na cells using different electrolytes through galvanostatic cycling at a current density of 1.0 mA cm^{-2} and a capacity of 1.0 mAh cm^{-2} at 25 °C. (a) PC, (b) THF, (c) 2-MeTHF and (d) 3-MeTHF.

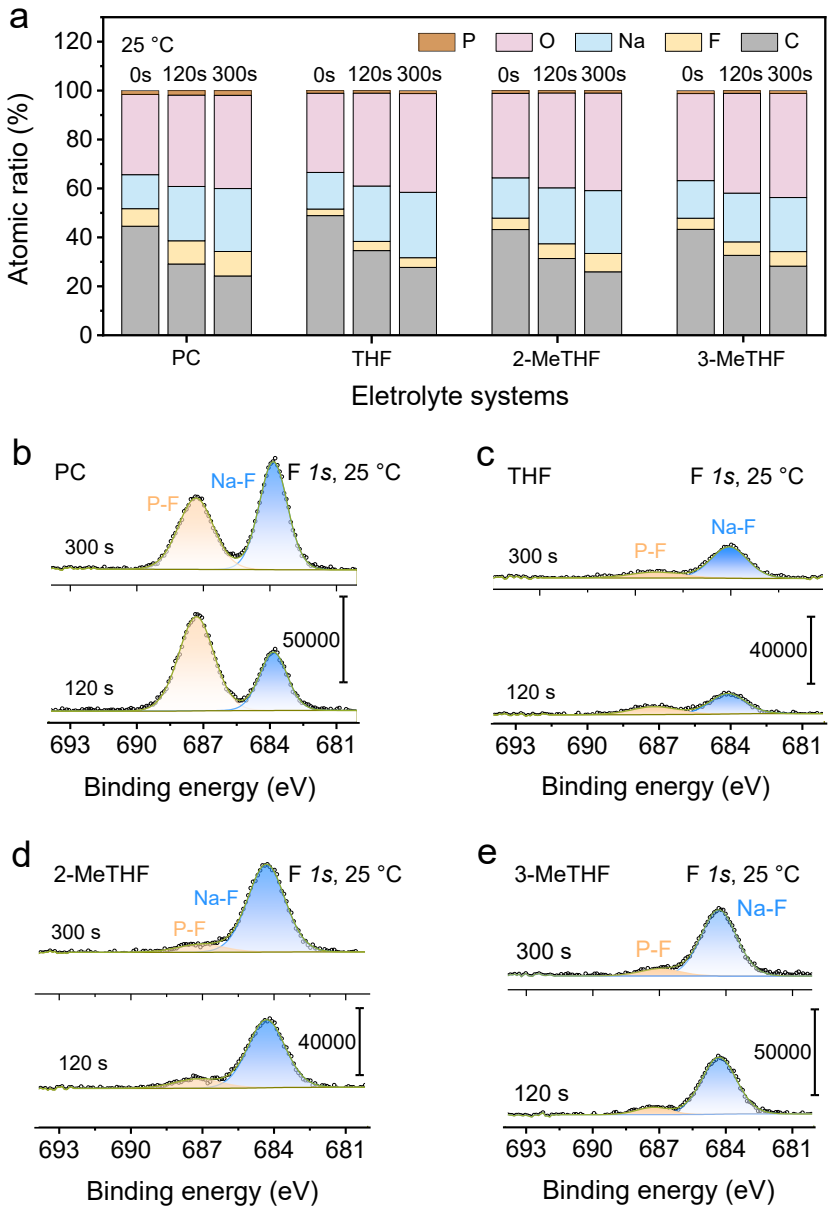

Supplementary Fig. 8 XPS depth profiling for the SEI layers formed on cycled Na metal negative electrodes in Na||NVP cells at discharged state after 100 cycles of 10C operation at 25 °C. (a) Depth-resolved atomic quantification within SEI layers, providing insights into the P/O/Na/F/C atomic distributions across sputtering depths. (b-e) The high-resolution XPS spectra of the F *1s* peak across different electrolytes: (b) PC, (c) THF, (d) 2-MeTHF and (e) 3-MeTHF electrolytes. These results reveal that the SEI in both 2-MeTHF and 3-MeTHF electrolytes exhibit a NaF-rich inner layer.

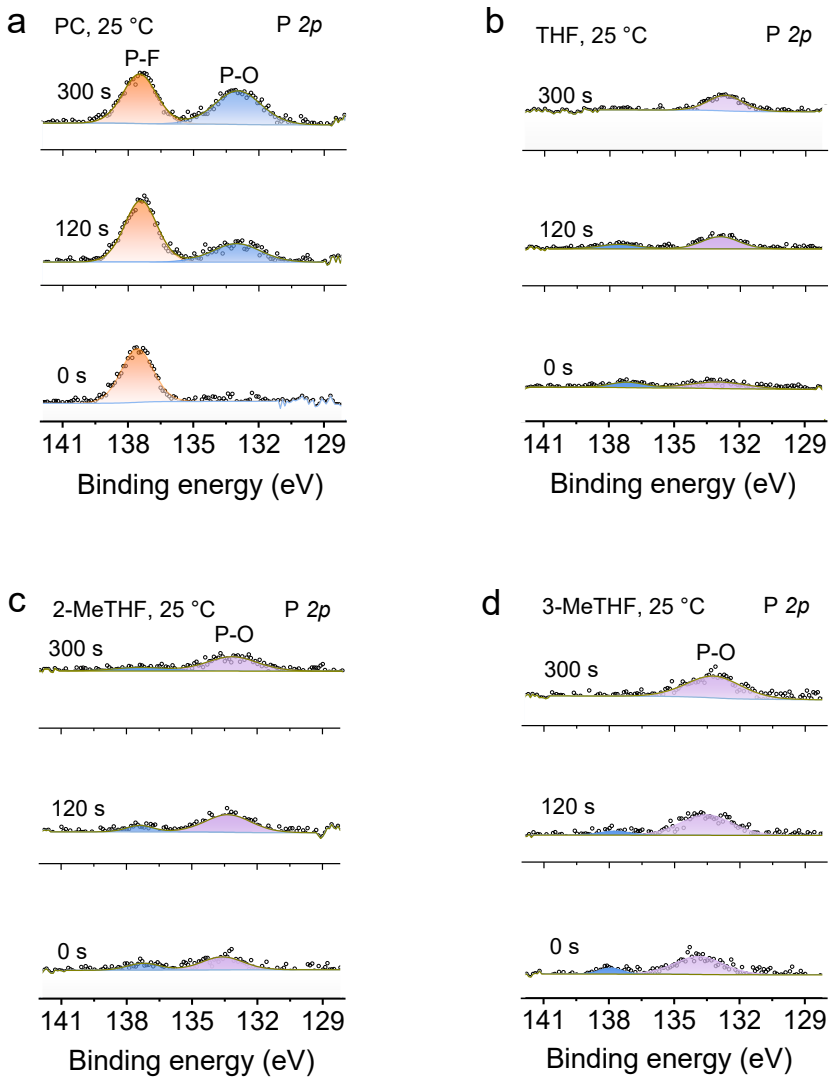

Supplementary Fig. 9 XPS depth profiling analysis of SEI layers on Na metal negative electrodes from Na||NVP cells at discharged state using the electrolytes after 100 cycles at 10C and 25 °C. (a-d) High-resolution XPS spectra of the P *2p* peak were deconvoluted with increasing sputtering time to investigate the evolution of the SEI in response to different electrolytes of PC (a), THF (b), 2-MeTHF (c) and 3-MeTHF (d), showing that the SEI derived from 3-MeTHF exhibited more significant anion decomposition, while the SEI from PC with more pronounced anion degradation.

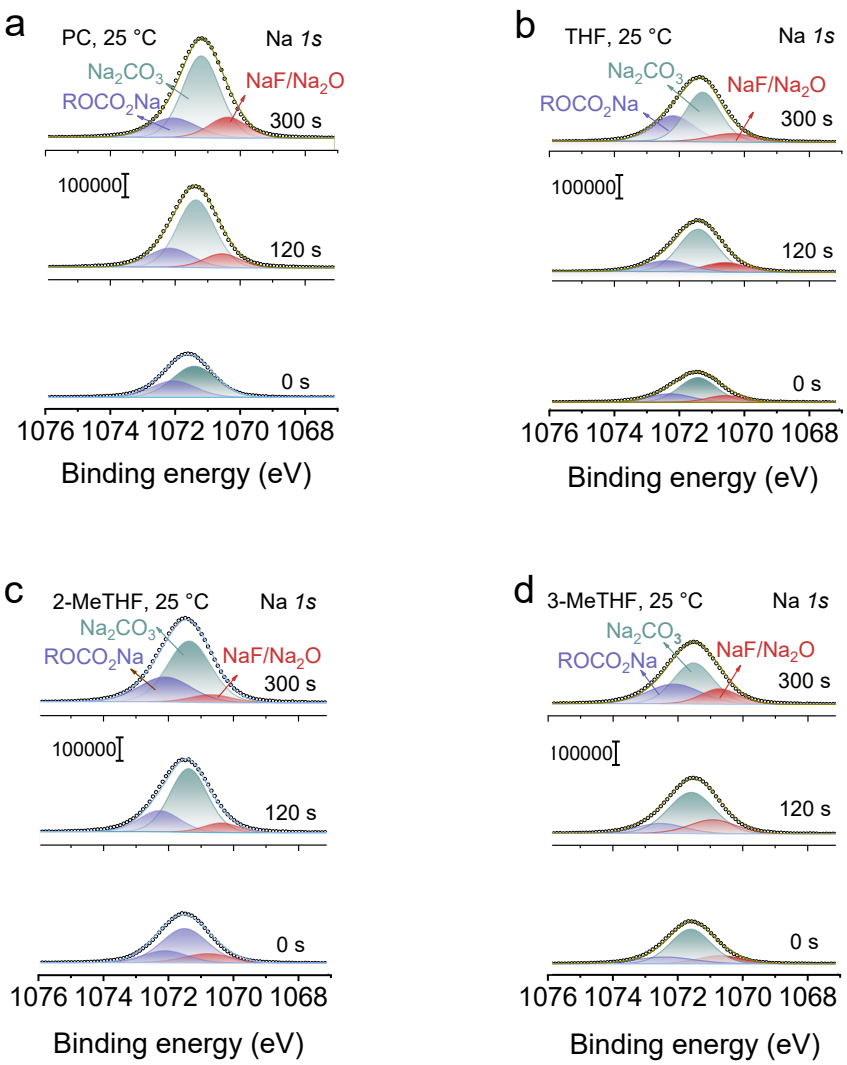

Supplementary Fig. 10 XPS depth profiling on cycled Na metal negative electrodes from Na||NVP cells at discharged state using different electrolytes after 100 cycles at 10C at 25 °C. (a-d) High-resolution spectral deconvolution of Na *1s* XPS spectra with progressive Ar_n^+ sputtering to investigate the different evolution of the negative electrode surface using electrolytes of PC (a), THF (b), 2-MeTHF (c) and 3-MeTHF (d).

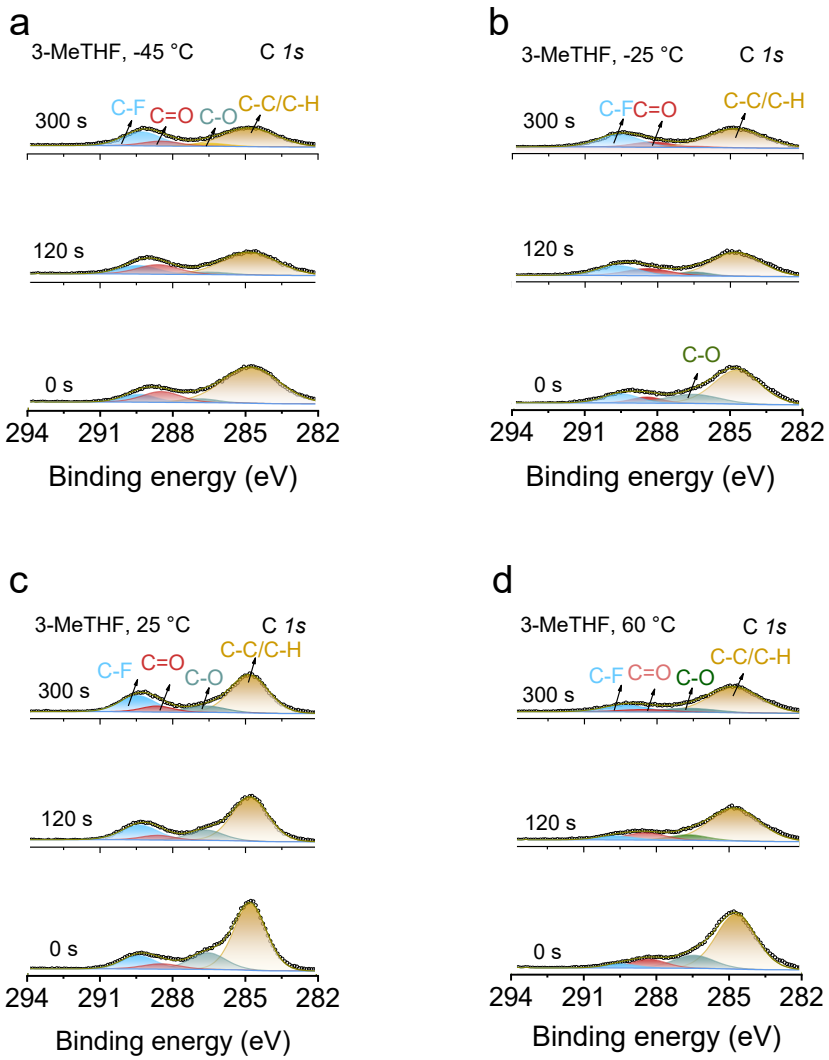

Supplementary Fig. 11 High-resolution XPS spectra of C *1s* fitted with increasing sputtering time to investigate the SEI layers formed by 3-MeTHF electrolyte. The temperature-dependent evolution of the C *1s* peak analyzed at the following temperatures: (a) −45 °C, (b) −25 °C, (c) 25 °C and (d) 60 °C, revealing the 3-MeTHF-derived SEI with weak C-C/C-H peaks at lower temperatures. The SEI layers on Na negative electrodes are from Na||NVP cells using 3-MeTHF electrolyte that were cycled at 10C for 100 cycles at discharged state.

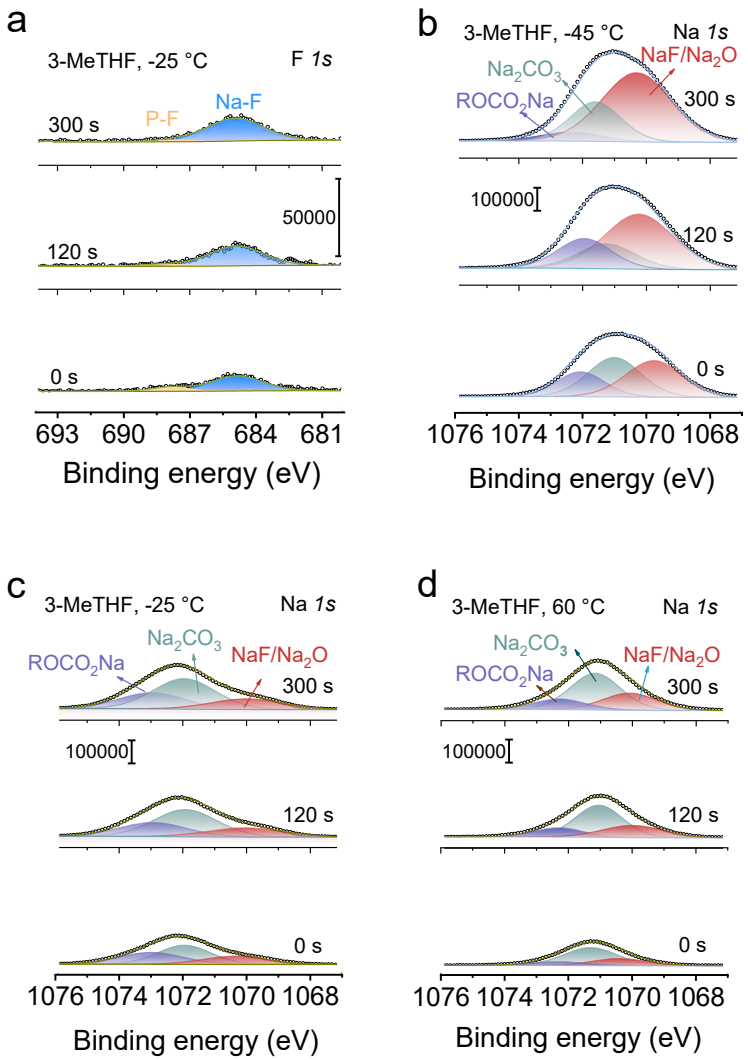

Supplementary Fig. 12 XPS depth profiling on discharged Na metal negative electrodes from Na||NVP cells using 3-MeTHF electrolyte after 100 cycles at a current rate of 10C under −25 °C and −45 °C. (a-d) High-resolution XPS spectra obtained with progressive Ar_n^+ sputtering to investigate the changes in the surface chemistry of the negative electrodes: (a) F *1s* XPS spectra of at −25 °C, and (b-d) Na *1s* XPS spectra at −45 °C (b), −25 °C (c), and 60 °C (d).

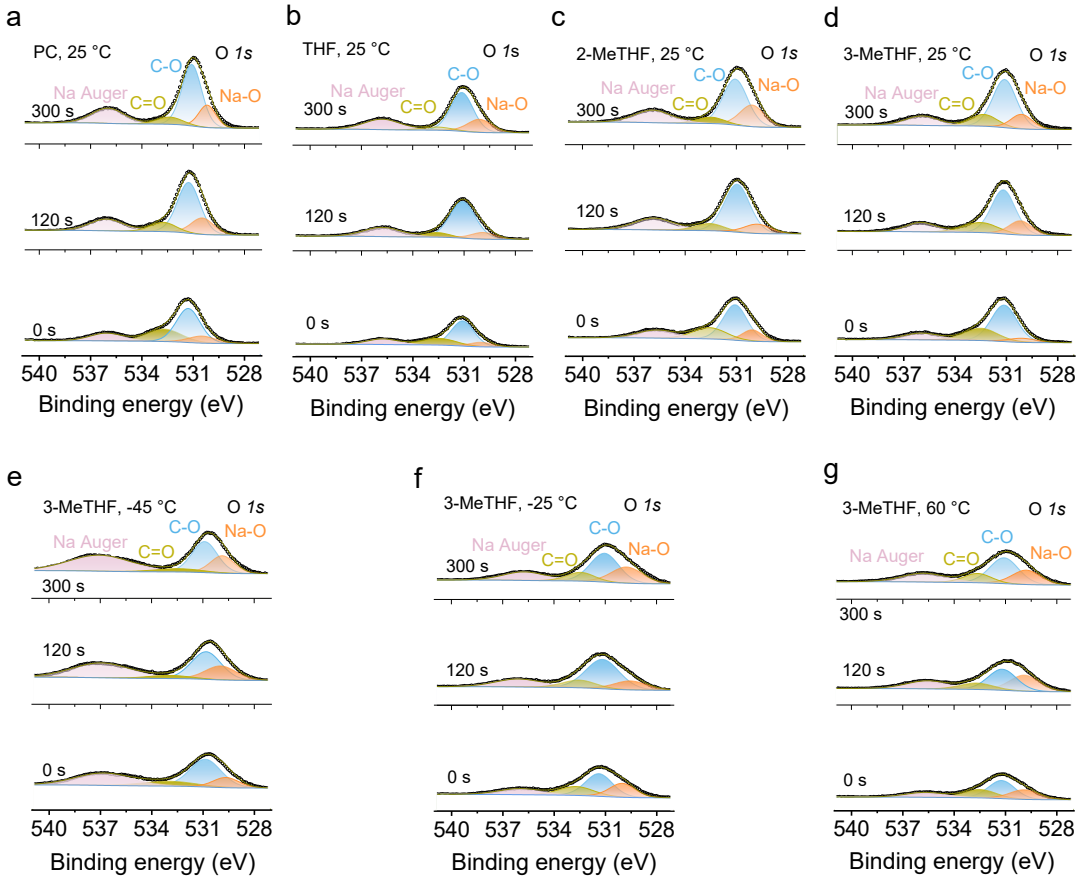

Supplementary Fig. 13 XPS depth profiling analysis of SEI layers on discharged Na negative electrodes from Na||NVP cells after 100 cycles at 10C. (a-d) The SEIs formed with PC (a), THF (b), 2-MeTHF (c) and 3-MeTHF (d) at 25 °C. (e-g) The SEIs formed with 3-MeTHF at −45 °C (e), −25 °C (f) and 60 °C (g).

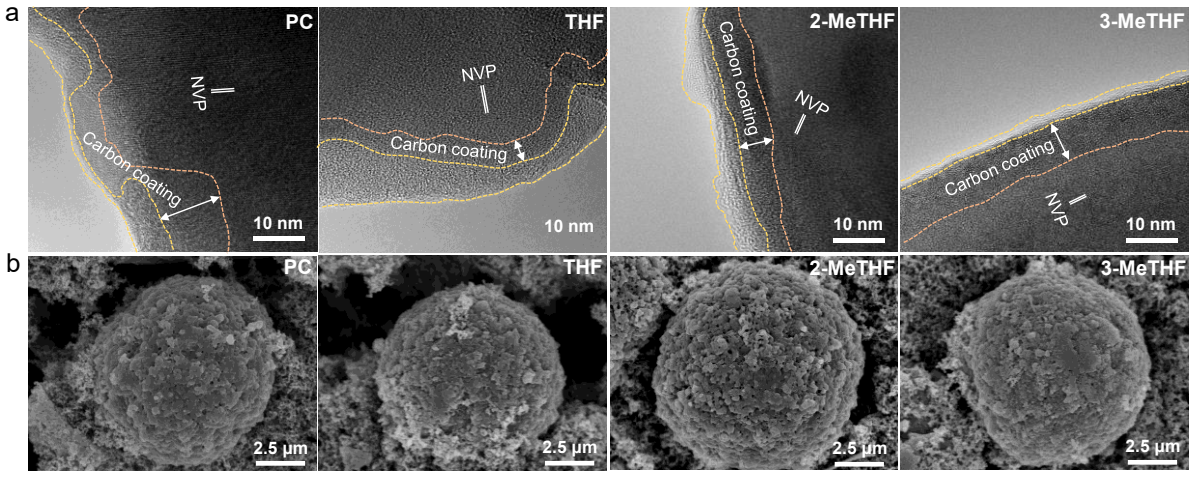

Supplementary Fig. 14 HR-TEM and SEM images of the discharged NVP positive electrodes from Na||NVP cells after 100 cycles at 10C and 25 °C. (a) HR-TEM and (b) SEM images. The colored dashed lines in (a) are used to outline the CEI layer on the cycled NVP positive electrodes. The spherical morphology of the NVP particles in the cells with different electrolytes remains well after cycling, while a thin and uniform CEI layer is formed by the 3-MeTHF electrolyte compared to those formed by other electrolytes.

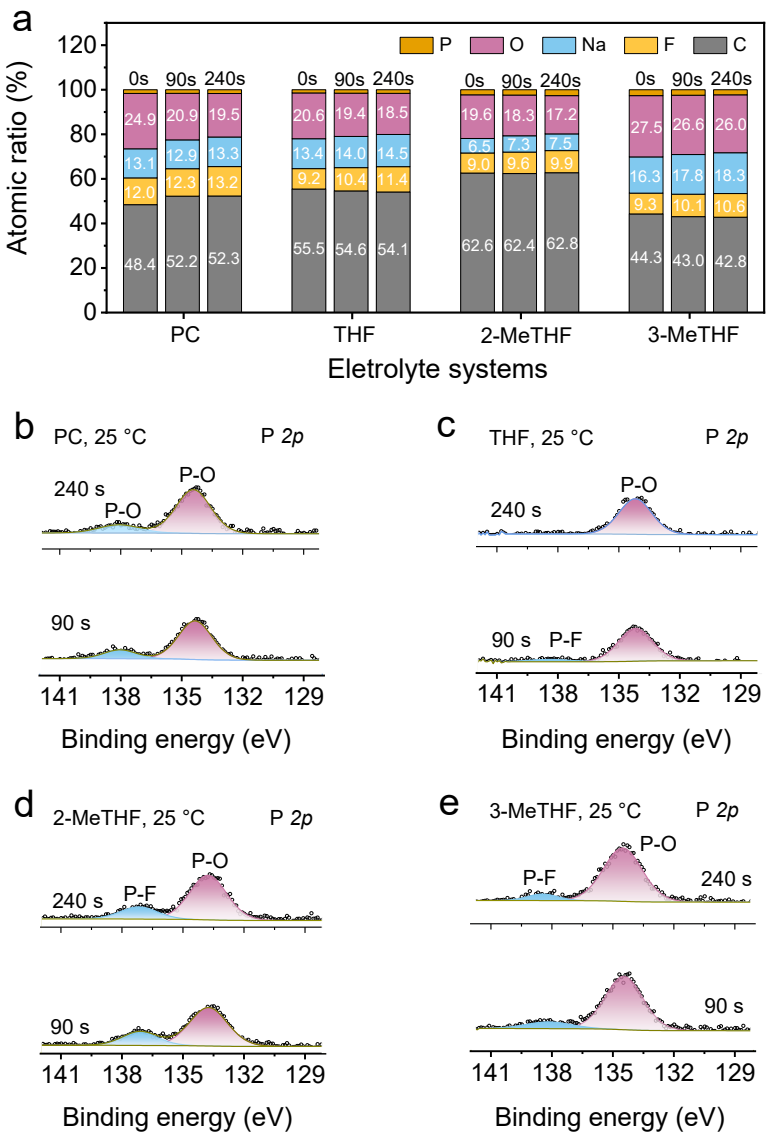

Supplementary Fig. 15 XPS depth profiling analysis of CEI layers on the discharged NVP positive electrodes performed across varying sputtering times at 25 °C. (a) The compositional quantification of elements including P, O, Na, F and C in the CEI layers on the cycled NVP positive electrodes at 25 °C. (b-e) The fitted high-resolution XPS spectra of P *2p* with increasing sputtering time to investigate the interfacial chemistry of the CEI formed with different electrolytes at 25 °C, revealing the 3-MeTHF derived CEI with anion-decomposition dominated interfacial chemistry: (b) PC, (c) THF, (d) 2-MeTHF and (e) 3-MeTHF. The Na||NVP cells using different electrolytes were cycled at 10C for 100 cycles.

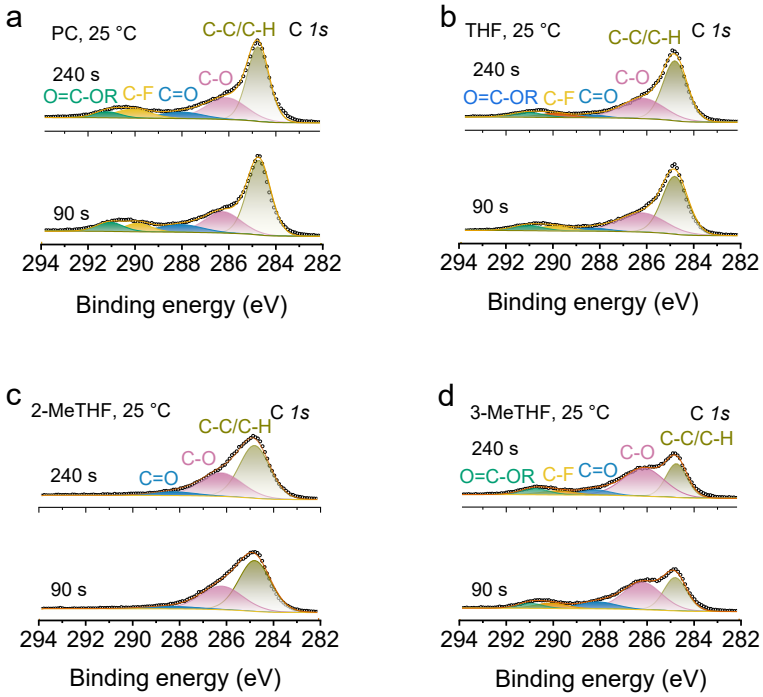

Supplementary Fig. 16 The fitted high-resolution XPS spectra of C *1s* with increased sputtering time for the CEI layers at 25 °C. (a-d) The spectra were obtained for the following electrolytes: (a) PC, (b) THF, (c) 2-MeTHF and (d) 3-MeTHF, providing a comparison of the electrolyte-dependent formation of the CEI and revealing the 3-MeTHF-derived CEI with weak C-C/C-H peaks. The Na||NVP cells at discharged state were cycled at 10C for 100 cycles at 25 °C using different electrolytes.

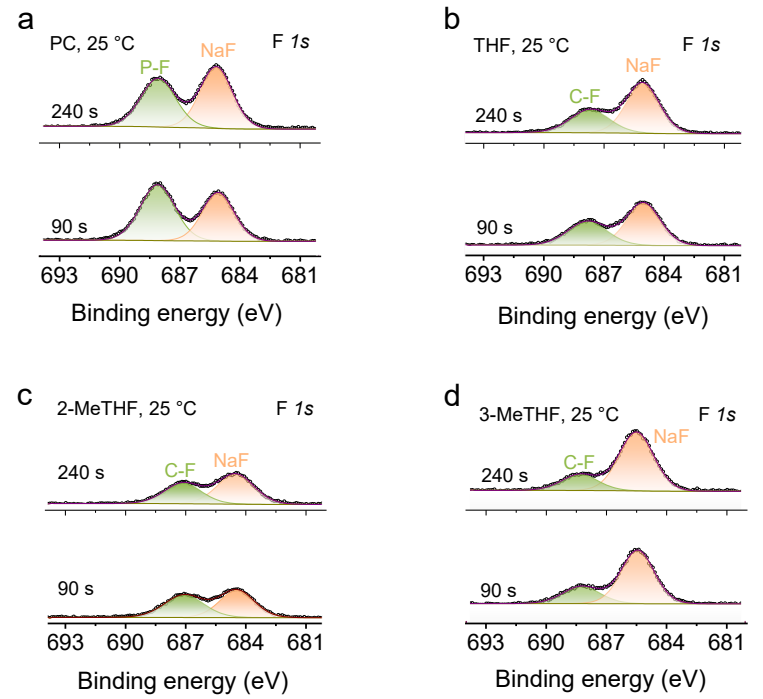

Supplementary Fig. 17 The fitted high-resolution XPS spectra of F *1s* with increased sputtering time for the CEI layers at 25 °C. (a-d) The SEI derived from PC (a), THF (b), 2-MeTHF (c) and 3-MeTHF (d) revealing the SEI derived from 3-MeTHF electrolyte with intensified NaF peaks. The Na||NVP cells at discharged state were cycled at 10C for 100 cycles at 25 °C using different electrolytes.

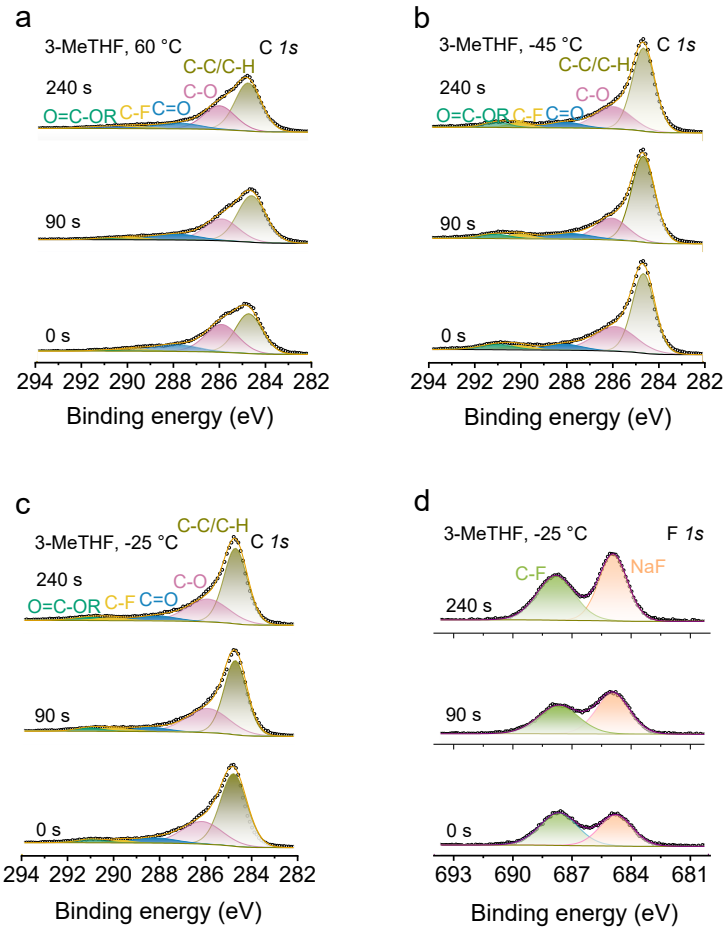

Supplementary Fig. 18 XPS depth profiling performed to analyze the discharged CEI derived from 3-MeTHF for 100 cycles at 10C at different temperatures. (a-c) Deconvoluted XPS spectra of C *1s* obtained with increasing sputtering time to investigate the evolving interfacial chemistry associated with the 3-MeTHF electrolyte at (a) 60 °C, (b)−45 °C and (c) −25 °C, providing insights into the impact of temperature on the composition and stability of the CEI during cycling. (d) The fitted high-resolution F *1s* XPS spectra through sputtering for the CEI layers from Na||NVP cell using 3-MeTHF electrolyte after 100 cycles at 10C under −25 °C.

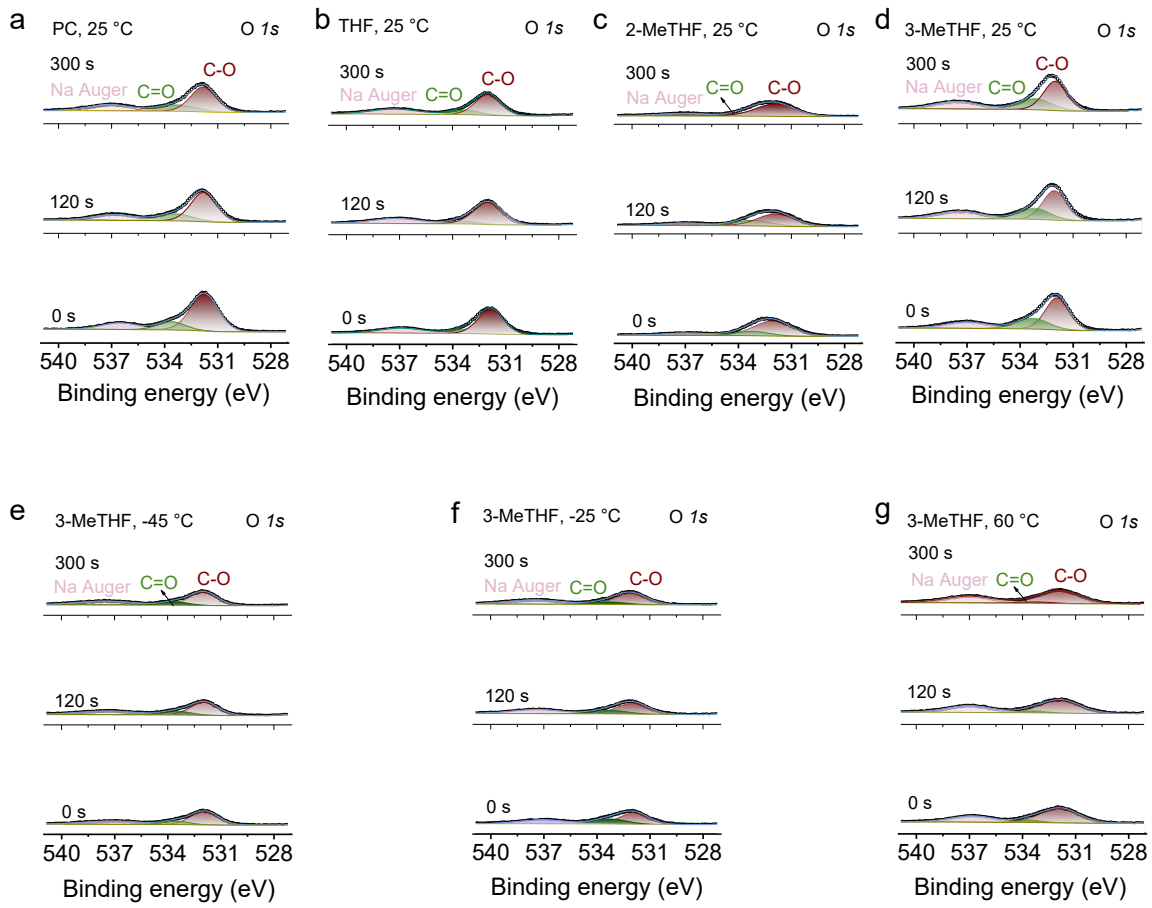

Supplementary Fig. 19 Deconvoluted XPS spectra of O *1s* for the CEI layers on positive electrodes from Na||NVP cells at discharged state using different electrolytes cycled at 10C for 100 cycles. (a-d) The CEIs formed with PC (a), THF (b), 2-MeTHF (c) and 3-MeTHF (d) at 25 °C. (e-g) The CEIs formed with 3-MeTHF at −45 °C (e), −25 °C (f) and 60 °C (g).

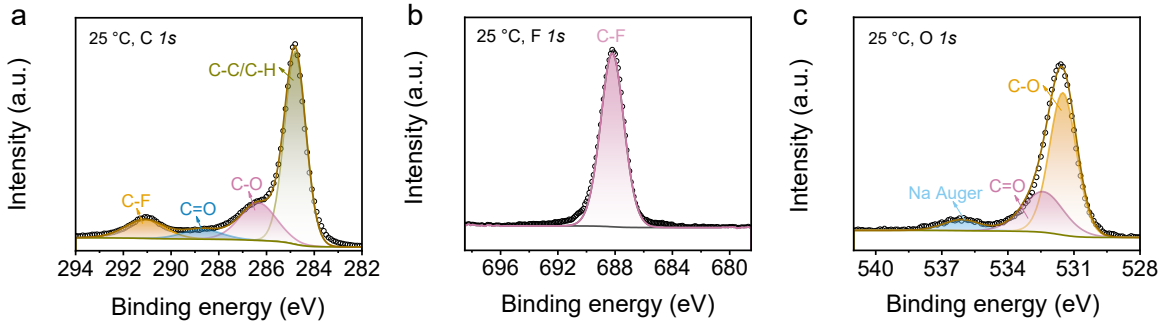

Supplementary Fig. 20 The XPS spectra collected to analyze the surface composition of the pristine NVP electrode prior to cycling. The spectra for the following elements are presented: (a) C *1s*, (b) F *1s* and (c) O *1s*, implying distinct differences between the fresh NVP electrode and the electrochemically altered surface chemistry observed in cycled ones.

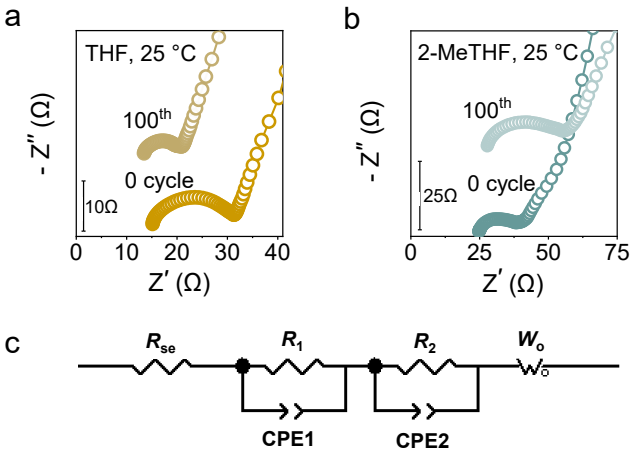

Supplementary Fig. 21 Evolution of electrochemical impedance spectroscopy (EIS) across electrolytes of THF and 2-MeTHF at 10C and 25 °C. (a, b) Nyquist plots showing distinct changes in interfacial resistance: (a) The impedance evolution of the cell with THF electrolyte. Note that THF shows a decrease in R_{cell} after 100 cycles, presumably due to the formation of organic-rich interphase that is conductive to the high ionic conductivity but shows low mechanical robustness. (b) A gradual increase in resistance in the cell with 2-MeTHF electrolyte, indicating a less favorable electrochemical interphase over cycling. (c) The equivalent circuit used for the data fitting.

Supplementary Table 2. The fitting results of the electrolyte resistance (R_s), interphase resistance ($R_{interphase}$) and charge-transfer resistance (R_{charge}) obtained for Na||NVP cells using different electrolytes over cycles at 10C and 25 °C. These results provide insight into the evolution of the interphases stability, highlighting the effects of electrolyte solvent selection on the overall cell performance during cycling.

Electrolyte	Cycle number	R_s (Ω)	Error (Ω)	$R_{interphase}$ (Ω)	R_{charge} (Ω)	Error (Ω)
PC	0	10.95	0.38	3.52	110.2	8.91
	100	9.27	0.16	126.6	1044	13.95
THF	0	16.27	0.31	3.14	9.00	3.69
	100	13.78	0.18	1.05	4.38	1.93
2-MeTHF	0	25.08	0.24	3.90	5.47	5.88
	100	28.08	0.30	5.50	14.85	5.41
3-MeTHF	0	15.44	2.65	6.42	3.43	1.51
	100	13.60	0.07	5.47	5.30	2.79

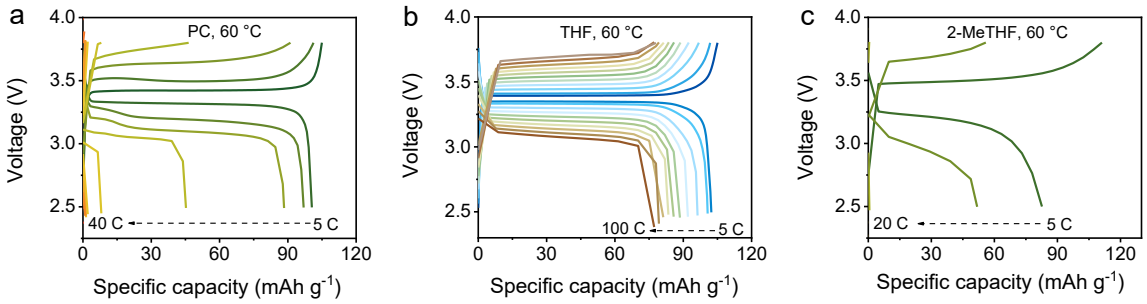

Supplementary Fig. 22 The evolution of the capacity-voltage profiles at rates from 5C to 100C for the Na||NVP cells using different electrolytes. (a-c) The comparison of the cells with PC (a), THF (b) and 2-MeTHF (c) electrolytes at 60 °C, showing the very limited rate capability in the cell with 2-MeTHF electrolyte due to the accelerated ring-opening decomposition at elevated temperature.

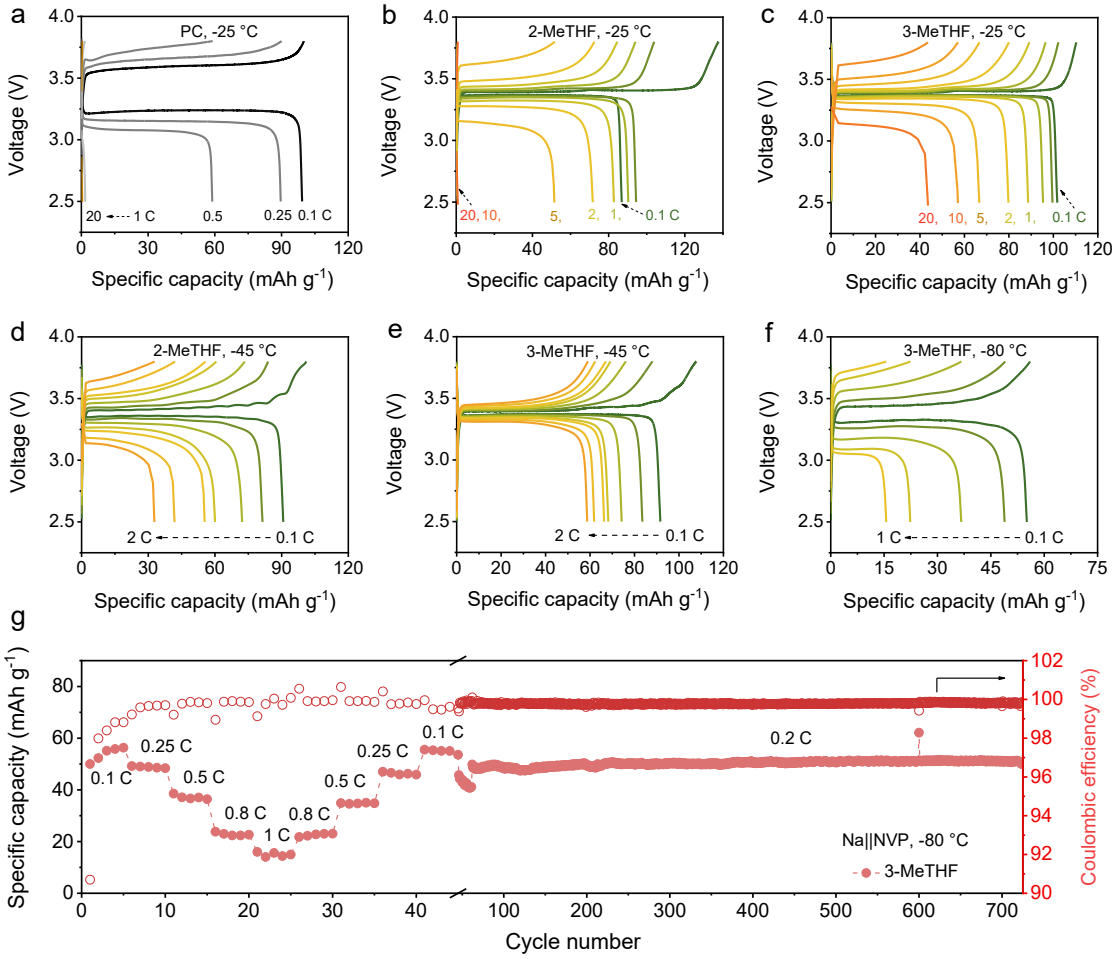

Supplementary Fig. 23 Electrochemical performance of Na||NVP cells evaluated at −25/−45/−80 °C using different electrolytes. (a-c) The charge/discharge profiles of Na||NVP cells with PC (a), 2-MeTHF (b) and 3-MeTHF (c) electrolytes. Notably, the 3-MeTHF electrolyte demonstrates high-rate capability, maintaining 45% of its initial capacity at 20C, outperforming both PC and 2-MeTHF electrolytes. (d-f) The charge/discharge profiles of Na||NVP cells with 2-MeTHF (d) and 3-MeTHF (e) electrolytes from 0.1C to 2C at −45 °C and Na||NVP cell 3-MeTHF from 0.1C to 1C at −80 °C (f). (g) The rate capability and the prolonged cycling stability of Na||NVP cells with 3-MeTHF at 0.2 C under −80 °C. Note that the unexpected increase in capacity (g) stems from unplanned temperature increases inside the testing chamber.

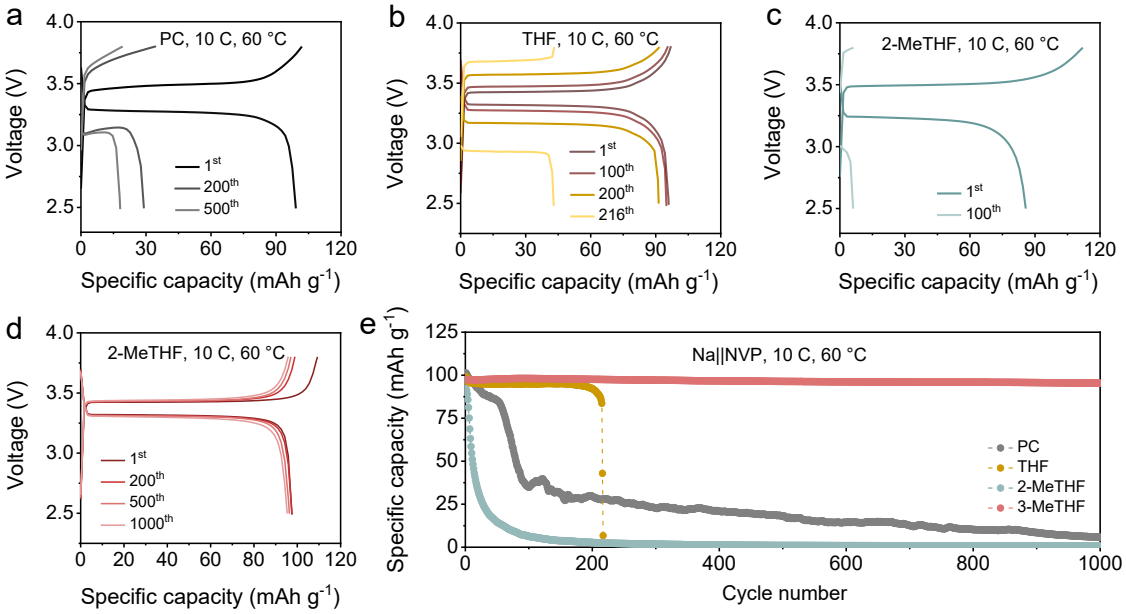

Supplementary Fig. 24 Comparison of long-term cycling performance of Na||NVP cells at 60 °C. (a-d) Capacity-voltage profiles for the cells testing at 10C by using PC (a), THF (b), 2-MeTHF (c) and 3-MeTHF (d). (e) Cycling stability of the cell using the PC, THF, 2-MeTHF and 3-MeTHF electrolytes.

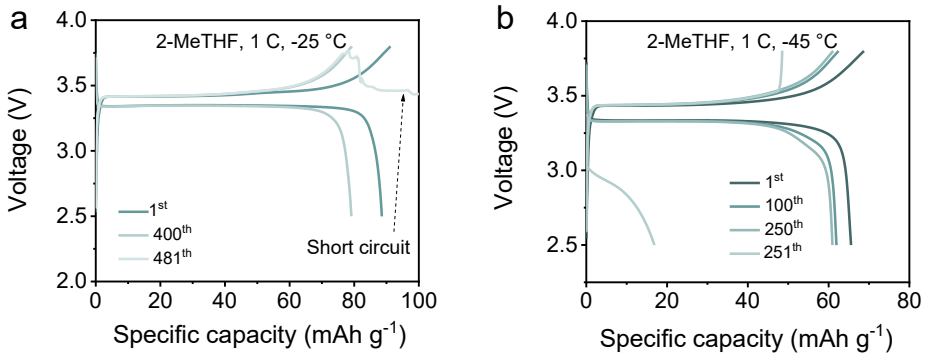

Supplementary Fig. 25 Galvanostatic charge-discharge profiles of Na||NVP cells using 2-MeTHF electrolyte and performed at 1C. (a, b) The cells displaying the occurrence of short circuits at both temperatures of −25 °C (a) and −45 °C (b).

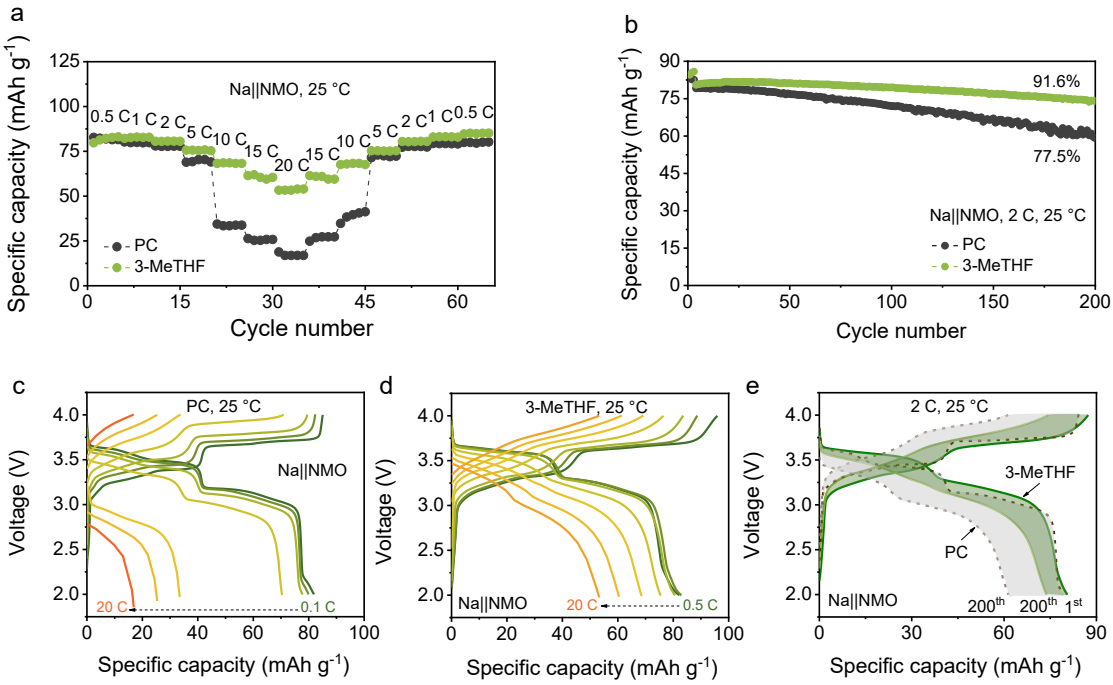

Supplementary Fig. 26 The electrochemical performance of Na||$Na_{2/3}Ni_{1/3}Mn_{2/3}O_2$ cells with PC and 3-MeTHF electrolytes. (a) Rate capabilities, (b) cycling stability, (c, d) capacity-voltage profiles of each rate for the cells with PC (c) and 3-MeTHF (d) and (e) capacity-voltage profiles for the cells at the 1st and 200th cycles. The $Na_{2/3}Ni_{1/3}Mn_{2/3}O_2$ is denoted as NMO (here, 1C = 100 mA h g^{-1} based on mass of NMO positive electrode).

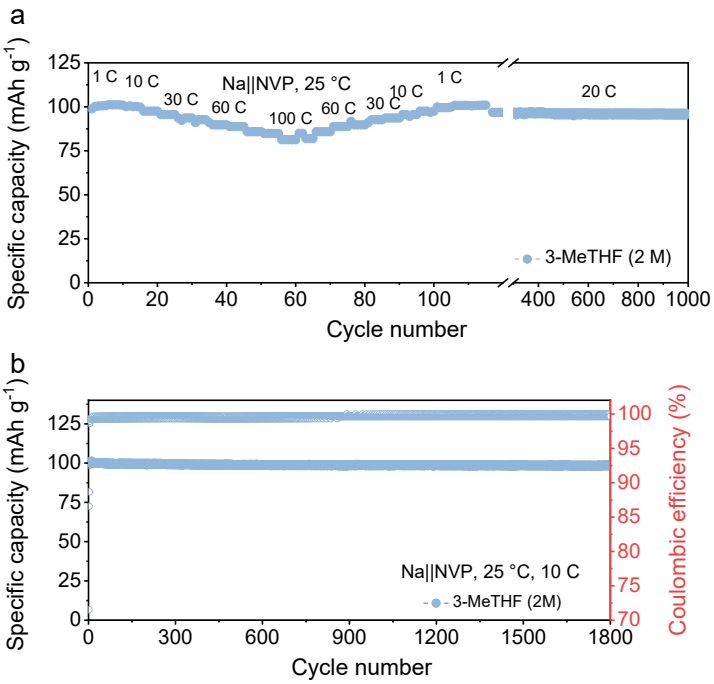

Supplementary Fig. 27 The electrochemical performance of Na||NVP cells with 2 M $NaPF_6$ in 3-MeTHF electrolyte at ambient temperature. (a) Rate capability and (b) cycling stability. Considering the economic benefit, the 1 M concentration was identified as an optimal balance in our design to provide the balanced Na^+-anions-solvent interaction for a stable, inorganic-rich SEI, while maintaining low enough viscosity and sufficient ionic conductivity to support fast charging and stable cycling.

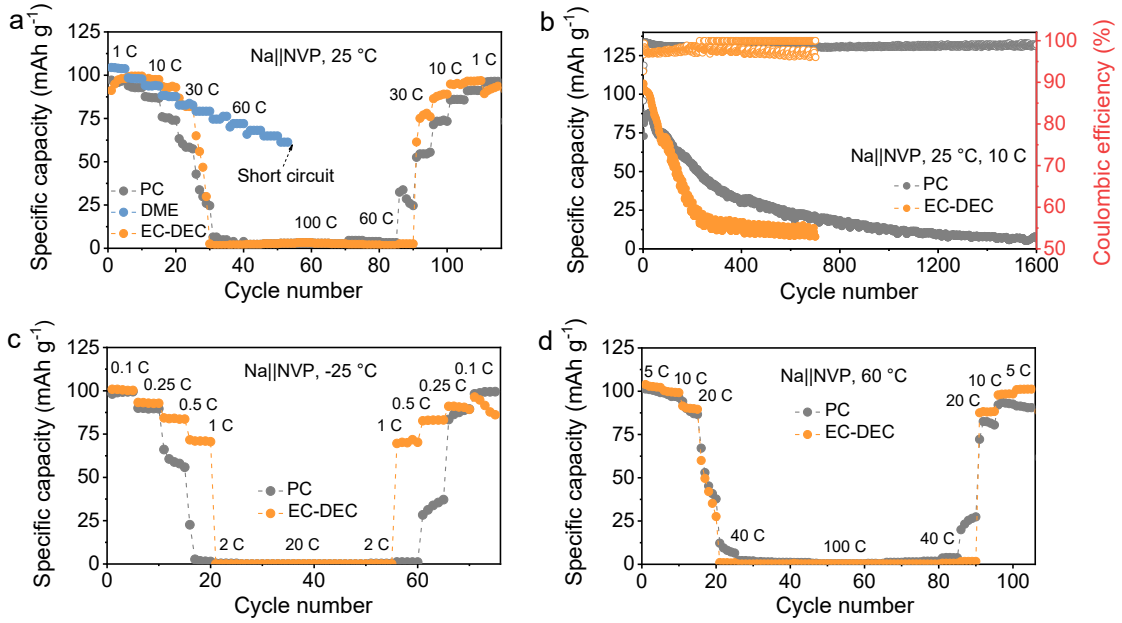

Supplementary Fig. 28 The electrochemical performance of Na||NVP cells with different baseline electrolytes. (a, c) Rate capability (a) and cycling stability (b) at 25 °C. (c, d) Rate capability at −25 °C (c) and at 60 °C (d).

Supplementary Note 4: Our rationale for selecting pure PC as the baseline is detailed as below. In view of scientific clarity in our work, a single, well-understood solvent is preferred to establish a clear structure-property relationship. Single PC solvent provides a simple and well-defined solvation environment, free from the complicated effects of multi-solvent coordination and preferential solvation that inherently exist in mixtures like ethylene carbonate (EC) and diethyl carbonate (DEC). This simplicity is crucial for investigating the fundamental interactions (Na^+-solvent and Na^+-anion) that are the central theme of our study. Further, in view of a rigorous benchmark for wide-temperature operation, PC is suitable for the wide-temperature performance due to its low melting point (−48.8 °C) and high boiling point (242 °C)[2,3]. Unlike the EC and DEC, they show high melting point of (EC: 36.4 °C) and low boiling point of (DEC:126 °C)[2,3].

In addition, we also evaluated the electrochemical performance of the cells with dimethoxyethane (DME) and EC-DEC for comparison, as shown in Supplementary Figure 28. The cell with DME shows short circuit, a failure mode that is consistent with the poor interfacial stability observed in the THF electrolyte. At 25 °C and −25 °C, the cells with PC shows a slightly inferior rate capability to the EC-DEC electrolyte that benefits from the lower melting point and viscosity from DEC. However, the capacity fade in the cells with PC is slightly mitigated compared to that using EC-DEC. Thus, in terms of the core scheme of electrolyte design and comparison of the electrochemical performance, PC is the suitable baseline electrolyte in this work.

Supplementary references

1. Eshetu, G. G. *et al.* Electrolytes and interphases in sodium-based rechargeable batteries: Recent advances and perspectives. *Adv. Energy Mater.* **10**, 2000093 (2020).
2. Dong, X. *et al.* High-energy rechargeable metallic lithium battery at −70 °C enabled by a cosolvent electrolyte. *Angew. Chem. Int. Ed.* **58**, 5623-5627 (2019).
3. Yang, J. *et al.* Cyclable micron-sized silicon-based lithium-ion batteries at −40 °C enabled by temperature-dependent solvation regulation. *Adv. Mater.* 2501807 (2025).
4. Zhou, P., Xiang, Y. & Liu, K. Understanding and applying the donor number of electrolytes in lithium metal batteries. *Energy Environ. Sci.* **17**, 8057-8077 (2024).
5. Flamme, B. *et al.* Guidelines to design organic electrolytes for lithium-ion batteries: environmental impact, physicochemical and electrochemical properties. *Green Chem.* **19**, 1828-1849 (2017).
6. Li, X. *et al.* Fast Interfacial defluorination kinetics enables stable cycling of low-temperature lithium metal batteries. *J. Am. Chem. Soc.* **146**, 17023-17031 (2024).
7. Pina, J. *et al.* Excited-state proton transfer in indigo. *J. Phys. Chem. B* **121**, 2308-2318 (2017).
8. Zhang, H. *et al.* Cyclopentylmethyl ether, a non-fluorinated, weakly solvating and wide temperature solvent for high-performance lithium metal battery. *Angew. Chem. Int. Ed.* **62**, doi:10.1002/anie.202300771 (2023).
9. Zhang, H. *et al.* Loosely coordinating diluted highly concentrated electrolyte toward −60 °C Li metal batteries. *J. Energy Chem.* **90**, 380-387 (2024).
10. Ge, B. *et al.* Aggregate-dominated dilute electrolytes with low-temperature-resistant ion-conducting channels for highly reversible Na plating/stripping. *Adv. Mater.* **36**, 2408161 (2024).
11. Leverick, G. & Shao-Horn, Y. Controlling electrolyte properties and redox reactions using solvation and implications in battery functions: A mini-review. *Adv. Energy Mater.* **13**, 2204094 (2023).
12. Liang, H.-J. et al. Electrolyte chemistry toward ultrawide-temperature (−25 to 75 °C) sodium-ion batteries achieved by phosphorus/silicon-synergistic interphase manipulation. *J. Am. Chem. Soc.* **146**, 7295-7304, (2024).
13. Eshetu, G. G. *et al.* Electrolytes and interphases in sodium-based rechargeable batteries: Recent advances and perspectives. *Adv. Energy Mater.* **10**, 2000093 (2020).